Constitutive modeling of a laumontite-rich tight rock and the application to poromechanical analysis of deeply drilled wells

Sina Heidari [a], Biao Li [a,*], Antoine B. Jacquey [b], Bin Xu [c,d]

[a] Department of Building, Civil & Environmental Engineering, Concordia University, Montreal, Quebec, H3G 1M8, Canada
[b] Department of Civil, Geological and Mining Engineering, Polytechnique Montreal, Montreal, Quebec, H3T 1J4, Canada
[c] Department of Civil Engineering, Schulich School of Engineering University of Calgary, Calgary, Alberta, T2N 4V8, Canada
[d] Origin Geomechanics Inc, Calgary, T3H 0X6, Canada

ARTICLE INFO

ABSTRACT

Geological formations containing laumontite-rich rock are usually treated as problematic for geo-energy production projects because the presence of laumontite mineral can promote complex mechanical behaviors. Previous laboratory results indicate that rock formations with a higher laumontite content display severe stress sensitivity in poromechanical responses. With an increase in confining pressure, there is a transition from dilation to compression regime and the resulting localization styles range from shear dilation to compaction bands. In this study, we conduct finite element modeling of constitutive behaviors of rocks retrieved from the tight glutenite reservoir formation using a thermodynamic-consistent plasticity model. The shear dilation to compaction transition is well characterized. Poromechanical analysis is also conducted to analyze the plastic zone development around a borehole drilled in an over pressured reservoir. The simulated stress-paths of key points around the borehole are used to demonstrate the plastic strain development processes. The impact of in-situ stress on the wellbore stability is highlighted, and a comparison with the results from using the traditional plastic constitutive model is conducted.

1. Introduction

In deep geo-energy engineering, rock formations containing laumontite should be given special attention as drilling or hydraulic fracturing tend to have issues in such formations (Chen et al., 2020). Laumontite is a soft mineral containing chemical water and has a chemical formula of $Ca(AlSi_2O_6)_2 \cdot 4H_2O$. Laumontite was usually formed in unconsolidated sediments with the assistance of alkaline interstitial solutions. Through silicate diagenesis processes, laumontite can be transferred into other zeolite type of minerals (Bravo et al., 2017; Vernik, 1990; Zhang et al., 2016). It can occur as fracture infills or as a replacement mineral of plagioclase within a rock formation (Morrow and Byerlee, 1991; Solum et al., 2003), thus laumontite plays an important role in crustal fault zones (Baik et al., 2009; Evans and Chester, 1995; Vernik and Nur, 1992). Previous experimental data have indicated the structural sensitivity of laumontite under dry-wet cycles and pressure or temperature disturbances (Bravo et al., 2017; White et al., 2004). The geomechanical characteristics of reservoir rocks can be complex due to the presence of laumontite. Previous studies on soft mudrocks or fault gouge geomaterials, which are also abundant in chemical bound water, have documented their complex stress path dependent mechanical behaviors (An et al., 2021; Li and Wong, 2017; Zhang et al., 2022).

Currently, there are very limited studies focusing on the constitutive behavior of laumontite rich rocks. Some tight reservoir rocks containing laumontite (glutenite) were treated as brittle material because of the presence of large quantity of aggregates (Chen et al., 2020). The only experimental data (from the literature) on the pressure-dependent constitutive behavior of laumontite-rich reservoir rocks is from Yang et al. (2021), which show that the rock can display shear to compaction yield transition behaviors under an increasing confining pressure condition. A better characterization of the constitutive behavior is essential for wellbore stability analysis and hydraulic fracturing design in deep geo-energy engineering (Chen et al., 2012; Li et al., 2018; Wu et al., 2018). The study by Chen et al. (2012) highlights the importance of considering strain hardening/softening behavior in poromechanical analysis of wellbore stabilities. Failure functions with multi-yield surfaces are usually considered in modeling complex constitutive behavior (Abaqus, 2016). However, a challenging aspect of such approach is how

---

Box 1
Summary of the algorithm to update the stress for visco-plastic constitutive law, modified after Jacquey et al. (2021).

1 Set $i = 0$, $\dot{\varepsilon}_v^p = 0$, $\dot{\gamma}^p = 0$, $R_v^{(0)} = R_v(0,0)$, $R_d^{(0)} = R_d(0,0)$;

2 While $i \leq i_{\max}$ **do**

3   **While** $\sqrt{R_v^{(i)2} + R_d^{(i)2}} > tol$ **do**

4   Compute $\delta\dot{\varepsilon}_v^{p(i+1)}$, and $\delta\dot{\gamma}^{p(i+1)} \rightarrow$ Eq.10

5   Update strain rates $\dot{\varepsilon}_v^{p(i+1)}$, and $\dot{\gamma}^{p(i+1)} \rightarrow$ Eq.11

6   Update residuals:

7 $R_v^{(i+1)} = R_v\left(\dot{\varepsilon}_v^{p(i+1)}, \dot{\gamma}^{p(i+1)}\right)$;
   $R_d^{(i+1)} = R_d\left(\dot{\varepsilon}_v^{p(i+1)}, \dot{\gamma}^{p(i+1)}\right)$;

8   **End**

9 $i = i + 1$;

10 End

the intersection of multiple yield functions is handled in the numerical implementation. Previous constitutive models on confining pressure dependent stress-strain rock behaviors are mostly applicable for brittle rocks and the attentions are mainly focused on the transition of tensile or shear failure mechanisms (Mukherjee et al., 2017; Zhu and Shao, 2017). In addition, in order to fulfill the second law of thermodynamics, most constitutive models consider an associate flow rule, which overestimates the dilation behavior in simulating volumetric strains of geomaterials with strong heterogeneity in particle sizes (Jiang and Xie, 2011; Puzrin, 2012; Vermeer and De Borst, 1984; Zhu and Arson, 2014). In recent years, the plastic damage model has also been well considered in the thermodynamic framework to account for the damage evolution process in post-peak brittle–ductile characteristics (Zheng et al., 2022a, 2022b). Another approach is to consider a constitutive model derived from a thermodynamic-consistent physical framework to capture the macroscopic evolution of deformation whether within dilation-enhanced brittle conditions or compaction-induced ductile conditions (Jacquey et al., 2021; Jacquey and Regenauer-Lieb, 2021).

In this study, we present the petrophysical and geomechanical characterization of a laumontite-rich tight rock with cores retrieved from a deep over-pressured petroleum reservoir. Using a thermomechanics-based viscoplastic (VP) model, we capture the confining pressure dependent constitutive behavior based on finite element modeling. We also extend the application to the poromechanical analysis of deeply drilled wells in an over pressured reservoir.

2. Constitutive model and governing equations for poromechanical analysis

2.1. A thermomechanics-based viscoplastic model

A new thermomechanics-based viscoplastic model proposed by Jacquey and Regenauer-Lieb (2021) is used herein to carry out the constitutive modeling of the deformation of laumontite-rich tight rock. The model is based on a thermodynamic-consistent physical framework and incorporates poromechanics of path- and rate-dependent critical state line models.

Before the introduction of the yield function and flow rule, we first introduce fundamental quantities of the constitutive model. For a hydromechanical coupled analysis, the negative or positive signs of stress and strain variables are usually expressed according to the convention of solid mechanics (tension is treated as positive). However, in order to be more comprehensive to display the internal variables (e.g., pre-consolidation stress and volumetric plastic strain) which are essential for describing the yield function and plastic flow behaviors, we use the following expressions to show the basic stress and strain invariants based on a triaxial setting:

$$p' = -\frac{\sigma'_{kk}}{3} \tag{1a}$$

$$q = \sqrt{\frac{3}{2}\tau : \tau} \tag{1b}$$

where p' is the effective stress (compression is treated as positive) and q the deviatoric stress (always positive by definition).

In Eq (1b) the deviatoric stress tensor τ is given as:

$$\tau_{ij} = \sigma'_{ij} + p'\delta_{ij} \tag{2}$$

In which σ' is the effective stress tensor, and δ_{ij} is the Kronecker delta.

The plastic volumetric strain ε_v^p (positive in compression), and the deviatoric or shear strain γ are expressed by:

$$\dot{\varepsilon}_v^p = -\dot{\varepsilon}_{kk}^p \tag{3a}$$

$$\dot{\gamma}^p = \sqrt{\frac{2}{3}\dot{e}_{ij}^p : \dot{e}_{ij}^p} \tag{3b}$$

A rate form has been given in Eq (3), and $\dot{e}_{ij}^p = \dot{\varepsilon}_{ij}^p + \frac{1}{3}\dot{\varepsilon}_v^p\delta_{ij}$ is the deviatoric plastic strain rate tensor.

According to Collins (2003), a general family of critical state line models based on the theory of thermomechanics can be generated by postulating a positive dissipation function.
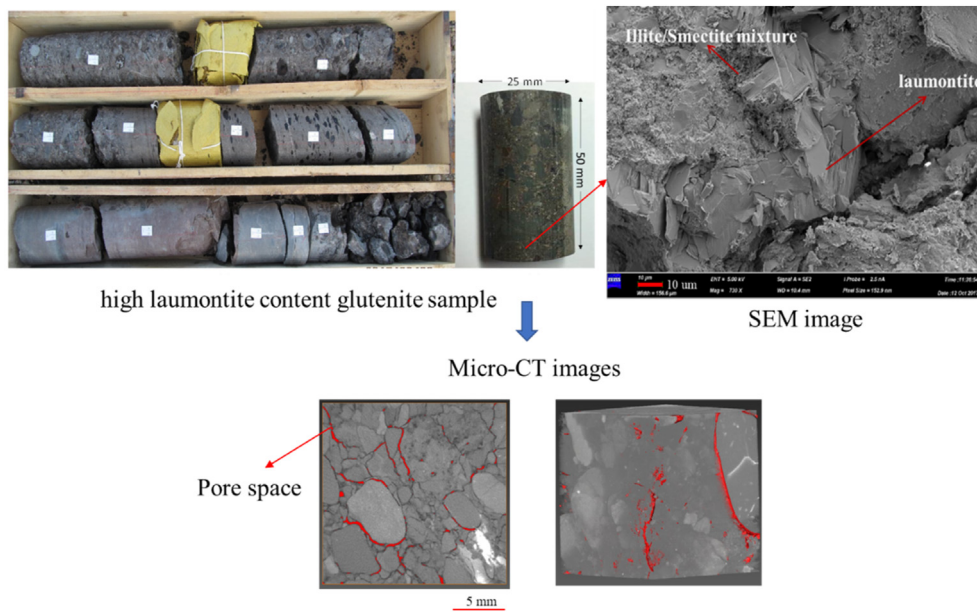
Fig. 1. Laumontite-rich tight rock cores used in this study along with the SEM image showing dominant minerals and micro-CT images showing pore structure.

Table 1

Mineralogy composition and porosity data of glutenite samples (average values are given for samples from the same well).

Sampling Depth(m)	Mineralogy composition by weight (%)					Porosity (%)
	Clay	Quartz	Feldspar	Calcite	Laumontite	
4000–4007	3.32	31.66	13.2	1.2	50.62	11.5

Table 2

Derived key parameters for the thermomechanics-based viscoplastic model based on triaxial test results.

Parameters	Values	Units
Initial critical pressure p_c^0	150	MPa
μ	1.25	–
α	0.45	–
γ	0.9	–

An essential aspect of this approach is the derivation of the yield function in the dissipative stress space, which takes a much simpler form than in the true stress space. Furthermore, Jacquey and Regenauer-Lieb (2021) extended within the thermomechanics framework the dissipation function introduced by Collins (2003) to consider rate dependent plastic deformation while maintaining the same yield function in the dissipation stress space, which reads:

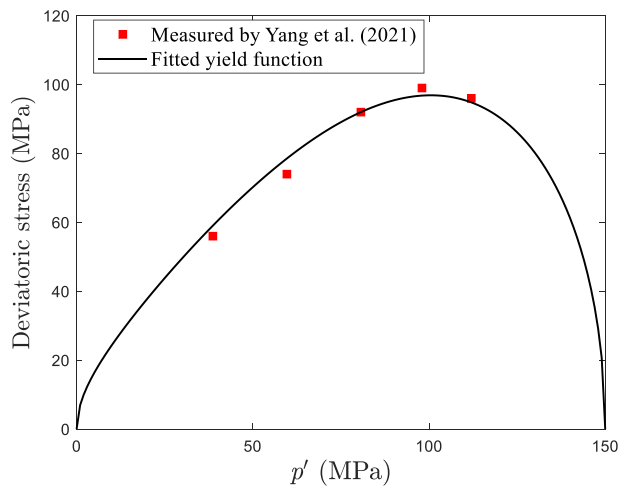$$F = \sqrt{\frac{\pi^2}{A^2} + \frac{\chi^2}{B^2}} - 1 = 0 \tag{4}$$

Fig. 2. Measured failure points and the fitted thermomechanics-based viscoplastic yield function of the laumontite rich rock based on triaxial test results.

where π is the effective dissipative stress, and χ is the dissipative deviatoric stress. This yield function consists of an ellipse of semi-axis A and B *centered in* $(0,0)$ in the effective dissipative stress space (π, χ). The coefficients A and B are given as:

$$A = (1-\gamma)p' + \frac{1}{2}\gamma p_c \tag{5a}$$

$$B = \mu\left[(1-\alpha)p' + \frac{1}{2}\alpha\gamma p_c\right] \tag{5b}$$

where μ is a material constant which is related to the rock's friction angle; α and γ are two dimensionless constants responsible for "dissipation coupling" and they guarantee on-associative flow rules in the true stress space. The transition from true stress space to dissipative stress space is given by:

$$p' = \rho + \pi \tag{6a}$$

$$q = \chi \tag{6b}$$

where ρ is the shift pressure which can be obtained as:

$$\rho = \frac{1}{2}\gamma p_c^0 \exp\left(\frac{\varepsilon_v^p}{\Lambda_i}\right) \tag{7}$$

In Eq (7), p_c^0 is the initial consolidation pressure, and Λ_i the plastic compressibility parameter that governs the inelastic compression or dilation behaviors.

Given the yield function expressed in Eq (4), the flow rules for the plastic strain invariants can be derived as:
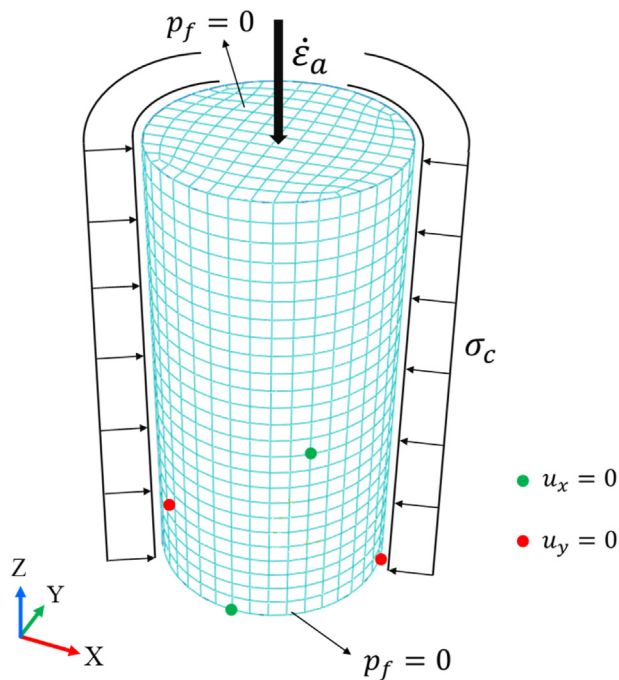
Fig. 3. Sketch showing the 3D finite element mesh along with the boundary conditions for the triaxial numerical test.

$$\dot{\varepsilon}_v^p = \frac{\langle F \rangle}{\eta} \frac{\partial F}{\partial \pi} \tag{8a}$$

$$\dot{\gamma}^p = \frac{\langle F \rangle}{\eta} \frac{\partial F}{\partial \chi} \tag{8b}$$

The flow rules shown in Eqs (8a) and (8b) are also expressed in the dissipative stress space, and a plastic strain rate vector normal to the yield function is formulated. η is a viscosity (or reference rate of dissipation) with specific units of pa^{-1}.s. The Macaulay brackets $\langle \bullet \rangle$ are applied to force the plastic strains to be always positive or null. As introduced in Eq (8), the flow rule for the plastic strain is orthogonal to the yield function in the dissipative stress space to fulfill the second law of thermodynamics. However, the flow direction is not necessarily orthogonal to the yield function in the true stress space, thus the use of dissipative stress can induce non-associative flow rules and therefore can better characterize the dilatancy behavior.

For viscoplastic constitutive laws, the yield function is first evaluated using trial effective stress. If the yield function is positive, the following residuals in Eq (9) are used to solve for an acceptable value for the plastic strain rate tensor.

$$R_v(\dot{\varepsilon}^p, \dot{\gamma}^p) = \langle F \rangle \frac{\partial F}{\partial \pi} - \eta \dot{\varepsilon}_v^p = 0 \tag{9a}$$

$$R_d(\dot{\varepsilon}^p, \dot{\gamma}^p) = \langle F \rangle \frac{\partial F}{\partial \chi} - \eta \dot{\gamma}^p = 0 \tag{9b}$$

The increments of plastic strain rates are obtained by differentiating Eq (9) and using Newton-Raphson iterations (noted $i + 1$):

$$\frac{\partial R_v^{(i)}}{\partial \dot{\varepsilon}_v^p} \delta \dot{\varepsilon}_v^{p(i+1)} + \frac{\partial R_v^{(i)}}{\partial \dot{\gamma}^p} \delta \dot{\gamma}^{p(i+1)} = R_v^{(i)} \tag{10a}$$

$$\frac{\partial R_d^{(i)}}{\partial \dot{\varepsilon}_v^p} \delta \dot{\varepsilon}_v^{p(i+1)} + \frac{\partial R_d^{(i)}}{\partial \dot{\gamma}^p} \delta \dot{\gamma}^{p(i+1)} = R_d^{(i)} \tag{10b}$$

with the increments obtained, the plastic strain rates are updated at each iteration provided that the residuals R_v and R_d reach a tolerance value.

$$\dot{\varepsilon}_v^{p(i+1)} = \dot{\varepsilon}_v^{p(i)} + \delta \dot{\varepsilon}_v^{p(i+1)} \tag{11a}$$

$$\dot{\gamma}^{p(i+1)} = \dot{\gamma}^{p(i)} + \delta \dot{\gamma}^{p(i+1)} \tag{11b}$$

The procedure to update the effective stress tensor for viscoplastic constitutive laws is summarized in Box 1.

2.2. Poromechanical analysis

For a fully saturated rock, the poromechanical behavior can be generally described using theories of poroelasticity (Biot, 1956). Jacquey et al. (2021) extended a modular thermomechanics approach to include rate-dependent critical state line constitutive models for hydro-mechanical coupling as relevant for porous media. The partial differential equations for the mechanical response of skeleton and the evolution of the fluid pressure can be given as:

$$\nabla_j \cdot \left(\sigma_{ij}' - \alpha_B p_f \delta_{ij} \right) = 0 \tag{12}$$

$$\frac{1}{M_b} \frac{\partial p_f}{\partial t} + \alpha_B \frac{\partial \varepsilon_{kk}}{\partial t} + (1 - \alpha_B) \frac{\partial \varepsilon_{kk}^p}{\partial t} + \nabla \cdot \mathbf{q}_f = 0 \tag{13}$$

In Eqs (12) and (13) the Biot's poroelastic coefficient α_B and the Biot's modulus M_b are given as:

$$\alpha_B = 1 - \frac{K}{K_s} \tag{14}$$

$$\frac{1}{M_b} = \frac{n}{K_f} + \frac{(\alpha_B - n)}{K_s} \tag{15}$$

where p_f is the pore fluid pressure, n is the porosity, K is the drained bulk modulus of the rock with K_s the solid bulk modulus, and K_f the fluid bulk

Table 3
Poroelastic and viscoplastic parameters of laumontite rich rock samples used for triaxial numerical tests.

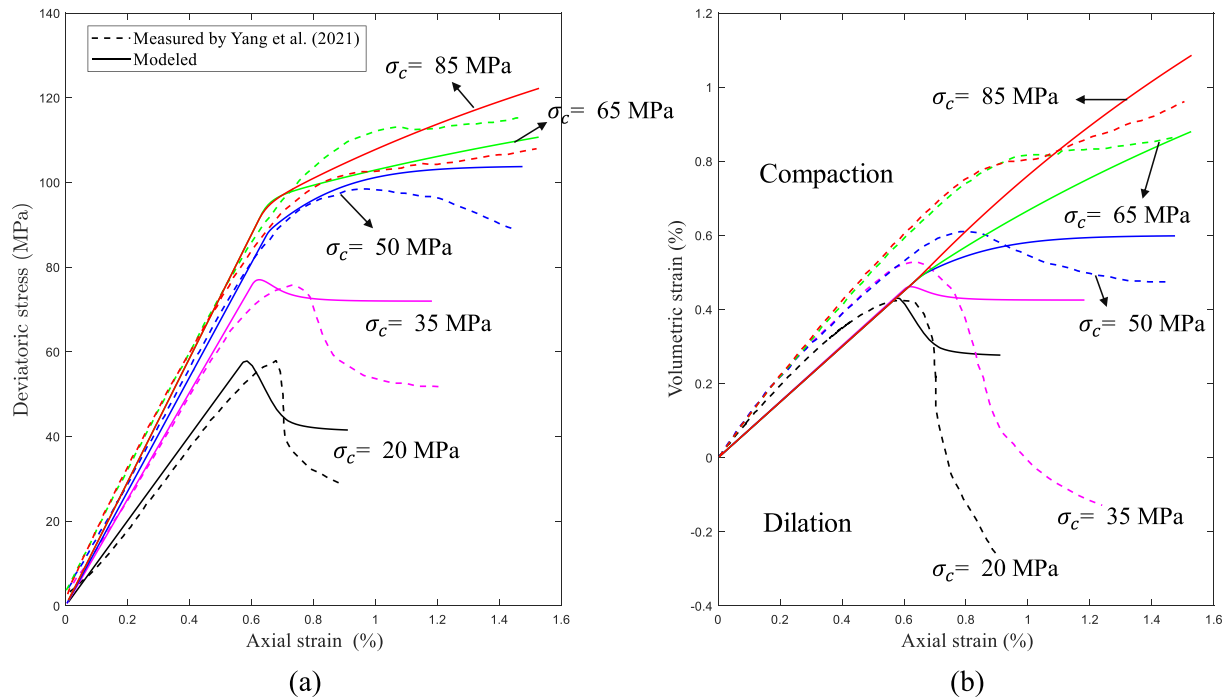| Parameters		Symbols	Values	Units
Young's modulus		E	12.6	GPa
Permeability		k	9.87×10^{-16}	m^2
Fluid bulk modulus		K_f	2	GPa
Fluid viscosity		μ_f	1×10^{-3}	Pa.s
Solid modulus		K_s	35	GPa
Porosity		n	0.11	–
Poisson's ratio		ν	0.2	–
Biot coefficient		α_B	0.8	
Plastic viscosity		η	2×10^{-5}	Pa^{-1}.s
Plastic compressibilities	Dilation	Λ_d	1×10^{-3}	–
	Compression	Λ_c	2×10^{-2}	

Fig. 4. Plots of measured and modeled (a) deviatoric stress and (b) volumetric strain versus axial strain for the laumontite rich rock samples under different confining pressures.
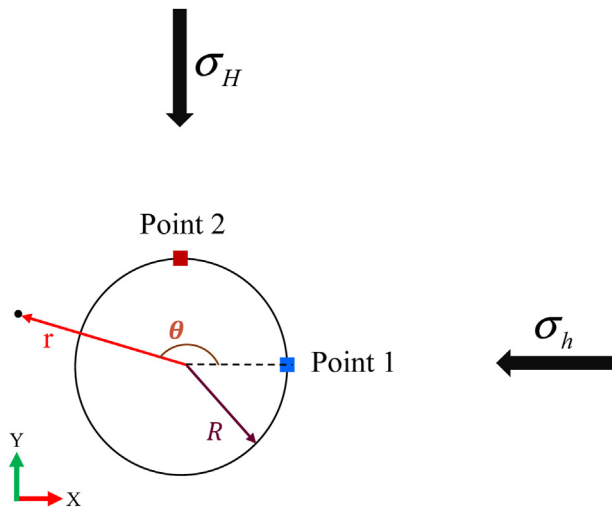

Fig. 5. Sketch showing in-situ stress directions along with the two monitoring points.

modulus. $\mathbf{q}_f$ is the Darcy velocity defined via the intrinsic permeability k and the fluid viscosity μ_f as:

$$\mathbf{q}_f = -\frac{k}{\mu_f} \nabla \cdot p_f \qquad (16)$$

ε_{kk} is the total volumetric strain and ε_{kk}^p is the plastic strain component of the volumetric strain.

The balance of porosity, n can be further obtained as:

$$\frac{\partial n}{\partial t} - (\alpha_B - n)\left(\frac{1}{K_s}\frac{\partial p_f}{\partial t} + \frac{\partial \varepsilon_{kk}}{\partial t}\right) - (1 - \alpha_B)\frac{\partial \varepsilon_{kk}^p}{\partial t} = 0 \qquad (17)$$

3. Laboratory characterizations and constitutive modeling

3.1. Laboratory characterizations

The laumontite-rich tight rock (glutenite) cores used in this study were collected from a vertical well located in Xinjiang oilfield, China. The formation has a buried depth of more than 4000 m. Petrophysical and mineralogical tests are conducted on cores to obtain the mineralogical compositions, porosity, and pore structure characteristics. Triaxial tests are conducted on some samples to investigate the mechanical responses under different confining pressures and drained stress path conditions.

Shown in Fig. 1, laumontite-rich glutenite samples drilled from the target formation are loose and fragile with poor sorting. Cylindrical samples (25 mm in diameter and 50 mm in length) were retrieved from raw cores using a wire cutting machine. In order to characterize the mineralogy compositions of studying laumontite-rich tight rock samples, we also carried out X-ray powder diffraction (XRD) analysis on collected specimens. The results of XRD are included in Table 1, which indicate that laumontite, quartz, and feldspar are the dominant minerals. There are also some clay minerals and calcite, where most of clay minerals are composed of swelling clay (I/S, illite/smectite mixture). The scanning electron microscope (SEM) analysis was also conducted and is displayed in Fig. 1. The result indicates that the high laumontite content glutenite has a plate-like mineral structure of laumontite surrounded by the illite/ smectite mixture. The Micro-CT image shows that pore space is mainly aligned around large aggregates. We also conducted the porosity measurement using N2 gas according to the approach of Boyle's law. In average, the studied rock has a porosity of 11.5%. But it should be noted that the chemical bound water takes up a certain amount of the pore space, thus the rock is treated as tight.

Triaxial compression tests on the rock samples were conducted by Yang et al. (2021) to investigate the geomechanical properties under different confining pressures. All the tested samples were loaded under a drained stress path condition, where drainage was provided on the
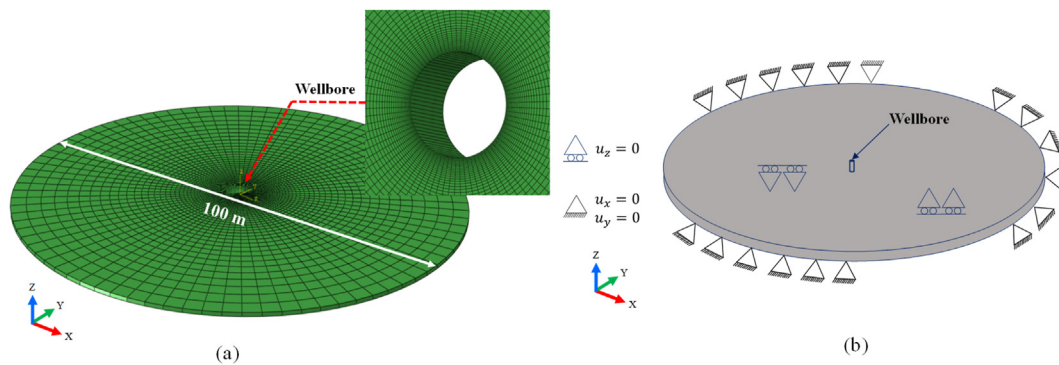
Fig. 6. Sketch showing (a) 3D mesh distribution and (b) boundary conditions for borehole stability analysis.

Table 4

In situ stresses and well geometry parameters of the borehole drilled in Xinjiang oilfield, China.

Parameters	Symbols	Values	Units
In situ stresses			
Vertical stress	σ_V	112.5	MPa
Maximum horizontal stress	σ_H	103.5	MPa
Minimum horizontal stress	σ_h	81	MPa
Wellbore			
Radius	R	0.216	m
Initial pore pressure	p_o	72	MPa
Mud density	ρ_w	1359	kg/m³
Depth	–	4500	m

bottom and top ends of the cylindrical sample. Local displacement transducers were applied to measure the axial and radial strains. Confining pressures (σ_C) of 20, 35, 50, 65 and 80 MPa were applied to different samples to investigate the stress-strain behaviors. Detailed information on the strength and deformation behavior will be elaborated along with simulated results in the subsequent section.

3.2. Triaxial test simulation and calibration

We collected the experimental data from Yang et al. (2021) and found out that samples display shear to compaction yield transition behaviors under an increasing confining pressure condition. By mapping the critical stress data in the stress space, we were able to gain information of the initial yield stresses based on the thermodynamic-based viscoplastic model presented previously. The results of studying laumontite-rich samples are shown in Fig. 2, where we illustrate the initial yield stress in the true stress space as derived from the critical stress at the onset of shear-enhanced compaction as published by Yang et al. (2021). The measured points shown in Fig. 2 correspond to the yield strengths beyond which volumetric strain starts going toward dilation. The fitted parameters of the yield function displayed in Fig. 2 are included in Table 2.

For simulating the deformation behavior of laumontite-rich samples under triaxial loading conditions, we make use of an open-source finite element method (FEM) numerical package called LEMUR (Jacquey et al., 2021) which includes an implementation of the thermomechanics-based viscoplastic model introduced in section 2. LEMUR was developed based on a high performance open-source FEM package with the Multi-physics Object Oriented Simulation Environment (MOOSE). Same as the laboratory tests by Yang et al. (2021), samples for the numerical tests also have a diameter of 25 mm and a height of 50 mm. The distribution of 3D mesh and the prescribed boundary conditions are illustrated in Fig. 3. The cylinder geometry is discretized into 3500 hexahedra elements. The poroelastic and the viscoplastic properties considered for triaxial calibration can be found in Table 3. A constant confining pressure is imposed on the vertical faces in the radial direction. The vertical displacement is

fixed on the bottom face of the cylinder while the lateral displacements are fixed on two points on the bottom face to avoid rotation of the cylinder. The axial loading is modeled by imposing a constant downward velocity on the top face. The axial strain rate of $\dot{\varepsilon}_a = 10^{-6}\,\text{s}^{-1}$ was applied for all models. Fluid pressure is held zero on the top and bottom faces to reproduce drained conditions.

Fig. 4 shows the simulation results of deviatoric stress and volumetric strain under drained triaxial loading conditions at different confining pressures. As shown in Fig. 4a for samples at confining pressures below 50 MPa the stress softening occurs after the peak strength, which indicates a brittle failure. Meanwhile, according to the volumetric axial strain curves presented in Fig. 4b, there is an apparent deflection of volumetric strain after entering the yield stage. After the peak strength, the volumetric strain decreases in the opposite direction as the axial strain increases, and shear dilation occurs. Under high confining pressure (above 50 MPa), the amplitude of stress increasing with axial strain decreases after yield point, which indicates the characteristics of stress hardening. The volumetric strain of rock continues to increase after the yield point, and shear-enhanced compaction occurs.

Generally, the simulated deviatoric stress vs. axial strain relations match well with the measured results. However, measured volumetric strain vs. axial strain relations are not well captured by our numerical tests (Fig. 4b). The compaction/dilation trend can be reproduced but the difference is more significant for cases with high confining pressures. During yield and failure processes, localization occurs within the rock samples. The dilation angle is known to be dependent on the particle size and in-homogeneity nature of disturbed samples. The present constitutive model focuses on the overall mechanical behavior of the simulated rocks from the macroscopic perspective; thus, a constant dilation angle is used in the simulation. For that reason, the changes in volumetric strain during the post-peak softening stage cannot be well characterized which can explain the discrepancies between modeling and experimental results. It is necessary to carry out micro-mechanical analysis in the mineral particle scale to understand the role of mineral geometry and heterogeneity on the overall rock mechanical behavior. Future work should focus on improving the current modeling approach when more experimental data are available for validations.

4. Poromechanical analysis of boreholes drilled in an over pressured reservoir

With the triaxial numerical test results, we proceed to conduct finite element numerical analysis of wellbores drilled in an over pressured reservoir, where laumontite-rich tight rocks are present. The poromechanical modeling is also based on the FEM package LEMUR. The numerical modeling is firstly validated using the available analytical solution for poroelastic analysis of boreholes drilled in a saturated porous media. Subsequently, plastic models are included to quantify the plastic yielding processes.
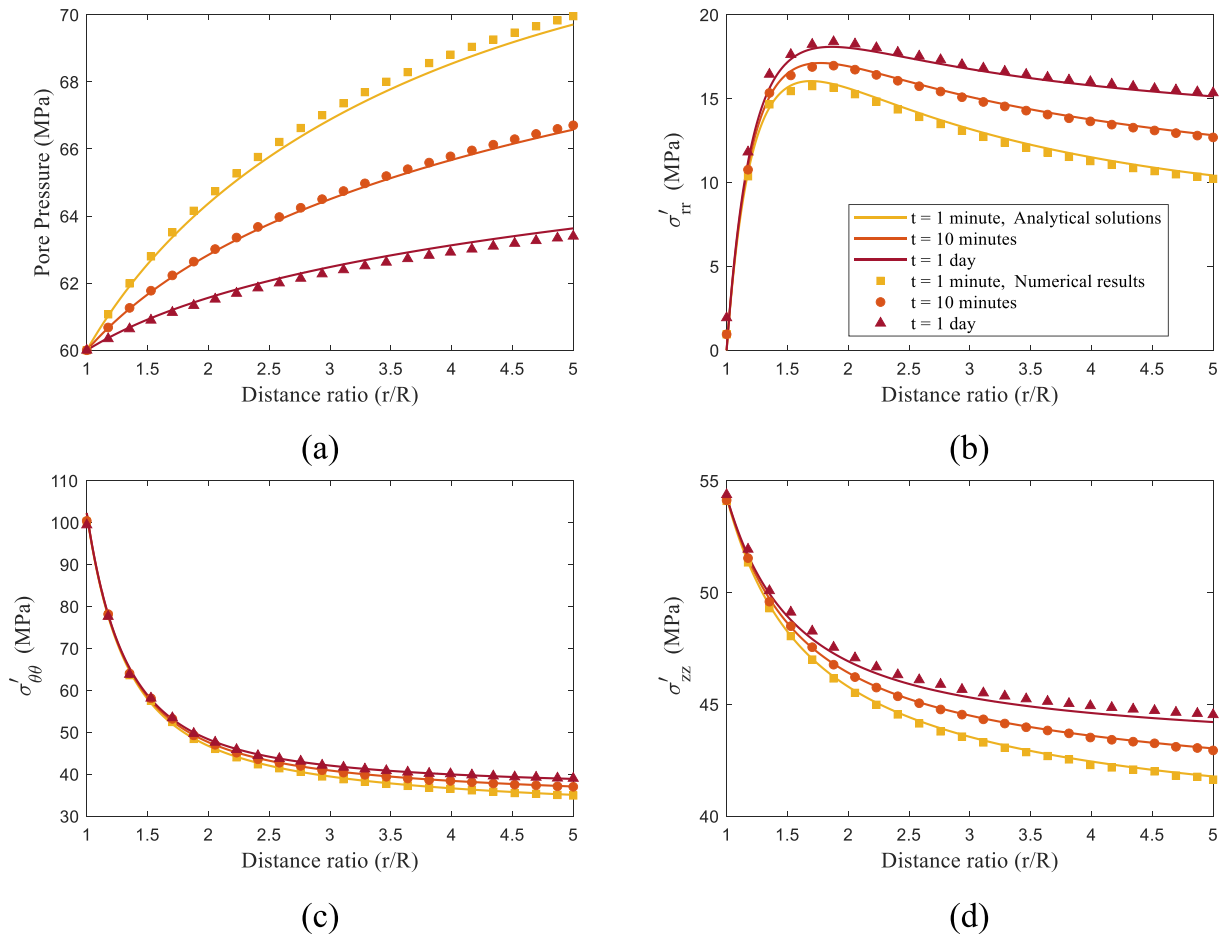
Fig. 7. Plots of analytical and modeled results of (a) pore pressure (b) effective radial stress (c) effective tangential stress and (d) effective vertical stress at different time.

Table 5
Summary of inputs for different cases of wellbore poromechanical analysis.

Cases	σ_V (MPa)	σ_H (MPa)	σ_h (MPa)	ρ_w (kg/m^3)	Plasticity model[a]
I	112.5	103.5	81	1379	VP
II	112.5	103.5	81	1485	VP
III	112.5	103.5	81	1585	VP
IV	112.5	103.5	70	1585	VP
V	112.5	103.5	70	1585	DP

[a] Note: VP = thermomechanics-based viscoplastic; DP = Drucker Prager.

4.1. Validation with analytical solution

The poromechanics/poroelastic analytical solution for stress and pore pressure distribution induced by the drilling in a saturated porous media, was presented by Abousleiman and Nguyen (2005). The analytical solutions were developed within the framework of the coupled processes for both single porosity and double porosity media which accounts for coupled isothermal fluid flow and rock/fractures deformation. The pore pressure field near the borehole is perturbed by the excavation. Fluid diffusion leads to a time-dependent redistribution of total and effective stresses. The plane-strain borehole problem can be decomposed into three individual problems: an elastic, a diffusion, and a poroelastic deviatoric stress loading problems (Cui et al., 1997). The complete solutions are obtained by superposition of the three individual problem solutions following decomposition of boundary conditions. The solution of mode 1 is purely elastic. The mode 2 is an uncoupled diffusion problem for pore pressure which is time dependent, whereas the solution of mode 3 involves a full poroelastic coupling.

The analytical solutions for a wellbore drilled in an infinite poroelastic medium, subjected to three-dimensional in situ state of stress and pore pressure are given as the following:

$$p_f = p_o + p_f^{(2)} + p_f^{(3)} \tag{18}$$

$$\sigma_{rr} = \sigma_m - \sigma_d \cos(2\theta) - \sigma_{rr}^{(1)} - \sigma_{rr}^{(2)} - \sigma_{rr}^{(3)} \tag{19}$$

$$\sigma_{\theta\theta} = \sigma_m + \sigma_d \cos(2\theta) - \sigma_{\theta\theta}^{(1)} - \sigma_{\theta\theta}^{(2)} - \sigma_{\theta\theta}^{(3)} \tag{20}$$

$$\sigma_{zz} = \sigma_V - 2v\sigma_m + v(\sigma_{rr} + \sigma_{\theta\theta}) + \alpha_B(1 - 2v)\left(p_f^{(2)} + p_f^{(3)}\right) \tag{21}$$

The solution of stress tensors in terms of cylindrical $\sigma_{rr}^{(1)}, \sigma_{rr}^{(2)}, \sigma_{rr}^{(3)}, \sigma_{\theta\theta}^{(1)}, \sigma_{\theta\theta}^{(2)}, \sigma_{\theta\theta}^{(3)}$ polar coordinates and pore pressures $p_f^{(2)}$, and $p_f^{(3)}$ are given in the Laplace domain and presented in the Appendix. The superscripts (1), (2), and (3) represent the solutions of the three loading modes of the modified plane strain problem. R is the radius of the well, r and θ are radial coordinates in the wellbore local coordinate. p_o denotes the original formation pore pressure before excavation. σ_H is the maximum horizontal stress, σ_h the minimum horizontal stress, and σ_V is the vertical stress. At the far field, when $r \rightarrow \infty$, the boundary conditions can be assumed around the domain as shown in Fig. 5.

The terms of σ_m, and σ_d are given as:

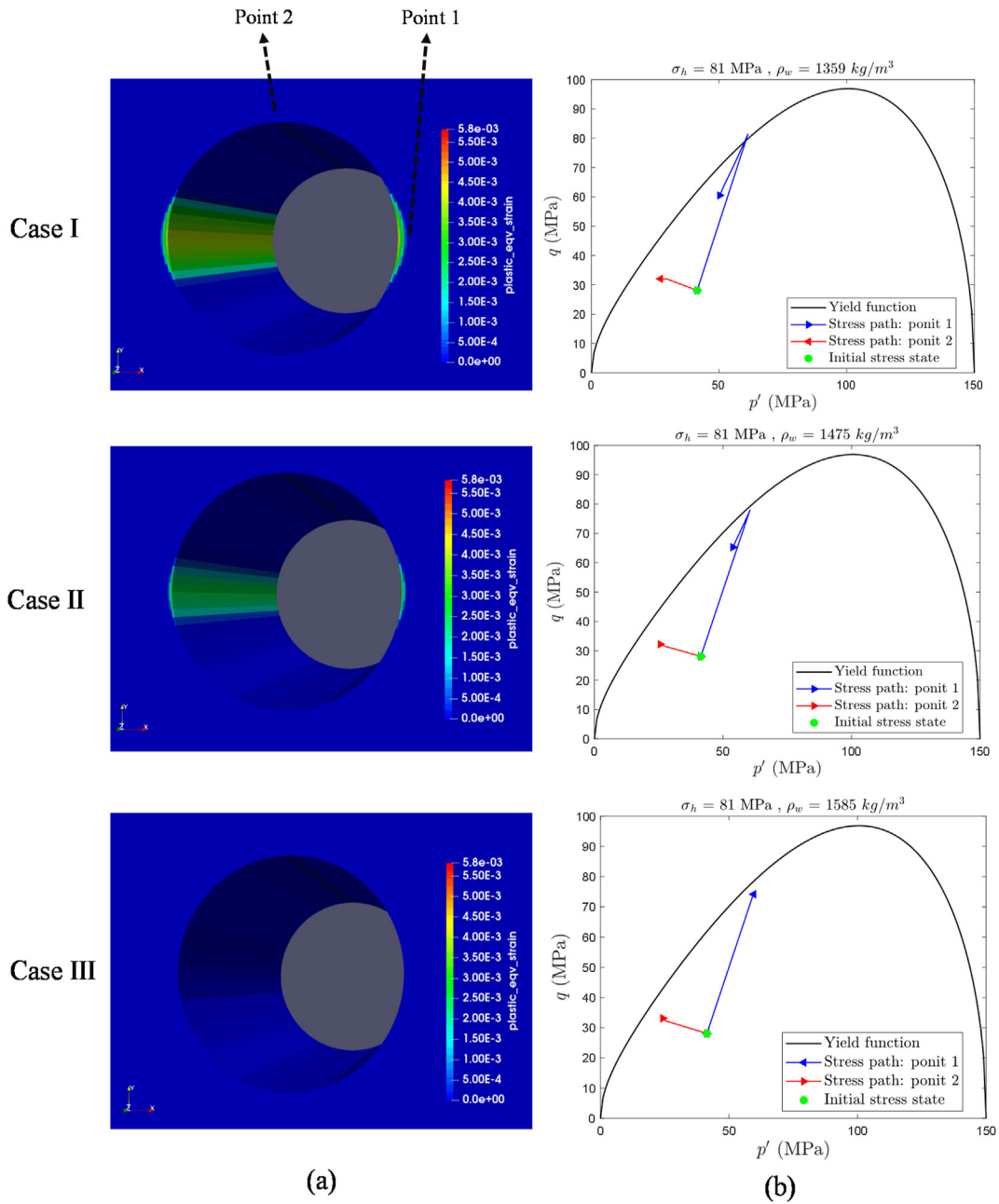$$\sigma_m = \frac{\sigma_H + \sigma_h}{2} \tag{22a}$$

Fig. 8. Plots showing: (a) accumulated plastic equivalent strain at t = 2 days under different drilling fluid pressures and (b) viscoplastic failure surface, stress paths of the selected points.

$$\sigma_d = \frac{\sigma_H - \sigma_h}{2} \tag{22b}$$

The prescribed boundary conditions and the domain size considered for the FEM numerical simulations are shown in Fig. 6. The depth of the wellbore was assumed to be 4500 m. The in-situ stresses and the wellbore geometry data are included in Table 4. The formation is over-pressured with a formation pressure gradient of 0.016 MPa/m. Information of in-situ stresses and formation pore pressure are according to Chen et al. (2020). The domain size around the wellbore was assumed to be 50 m which could be sufficient to ensure the negligible effect of the external boundaries. The mesh size is selected sufficiently small to consider detailed plastic deformation. The numerical model was first validated with 1359 kg/m^3 of mud density based on the single porosity solutions of Abousleiman and Nguyen (2005).

The solution in time is solved by a numerical inversion method

(Stehfest, 1970). The time domain solutions were put into implementation using MATLAB (Heidari et al., 2021). Fig. 7 illustrates the comparison between the analytical solutions and the corresponding pore pressure, effective radial, tangential, and vertical stresses obtained from the simulations along the radial direction when $\theta = 0$ at three different times. The agreement between the two solutions shows the convergence of the mesh size and the robustness of the FEM numerical package.

4.2. Numerical modeling using the thermomechanics-based viscoplastic model

We applied the thermomechanics-based viscoplastic model in the poro-elastic-plastic analysis of the deeply drilled well. In order to investigate the impacts of hardening/softening viscoplastic model on the plastic yield zones developed around boreholes, we choose a set of cases for the borehole stability analysis. Detailed description of each model is
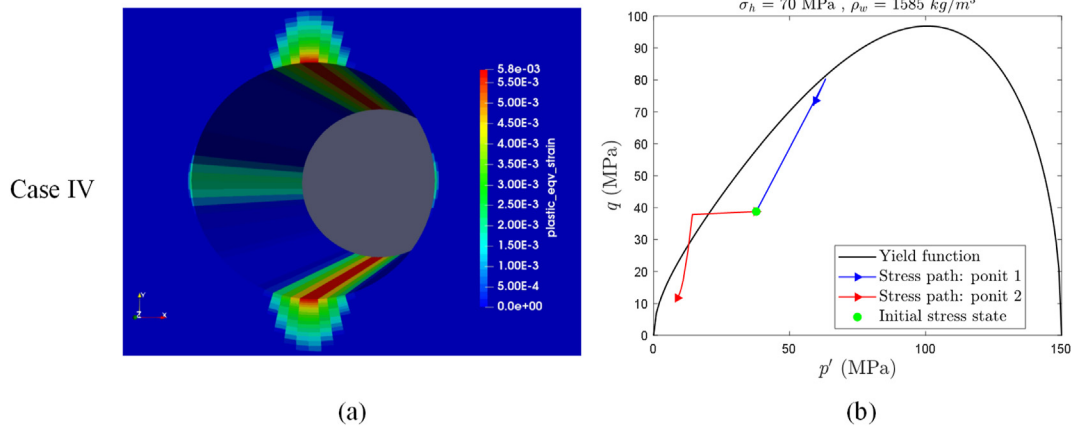
(a)

(b)

Fig. 9. Plots showing: (a) accumulated plastic equivalent strain and (b) stress paths of the selected points for a wellbore drilled in a formation with highly anisotropic in-situ stresses.
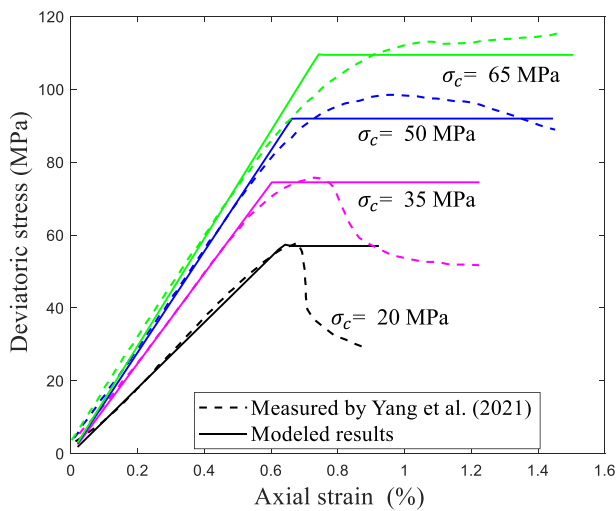

Fig. 10. Plots of measured and modeled deviatoric stress versus axial strain for the laumontite rich rock samples using the Drucker-Prager model.

summarized in Table 5. The well was analyzed under different mud pressures (with different drilling mud densities). Cases I, II, and III were chosen as initial models with three possible drilling mud densities to find out the reasonable value of the wellbore pressure. Other cases will be presented in the discussion section.

Fig. 8a shows the equivalent plastic strain distribution with three different fluid pressures. The results show that plastic zones are very significant in cases with mud densities of 1379 kg/m^3 and 1485 kg/m^3. Plastic zones are mainly developed around Point 1, which is in line with the direction of minimum horizontal stress (Fig. 5). A drilling mud with a density of $\rho_w = 1585$ kg/m^3 yields a safe well with no significant plastic strain developed around the borehole. As is show in Fig. 8b, the plastic yielding process for cases I and II can be illustrated by the effective stress paths of two selected monitoring points. The stress path for point 1 indicates an increase in the mean and deviatoric stresses and plastic yield is confirmed by the intersection with the yield surface. The softening stage is followed by a decrease in mean and deviatoric stresses. On the other hand, the stress path of point 2 continues to ascend towards but does not touch the failure surface. In addition, the mean effective stress for Point 2 always displays a decreasing trend.

5. Discussions

5.1. Impact of in situ stress

For a deep petroleum reservoir like the tight glutenite formation considered in this study, there are uncertainties in in-situ stress measurements. The variation of in-situ stress can be due to regional heterogeneity in lithology (Liu et al., 2022; Ma et al., 2022) or long-term petroleum production induced disturbance to the original in-situ stress (Chen et al., 2022). The impact of in-situ stress variation on wellbore stability was extensively studied in the literature (Abdollahipour et al., 2019; Hu et al., 2018). Shown in Table 5, we will consider a possible case
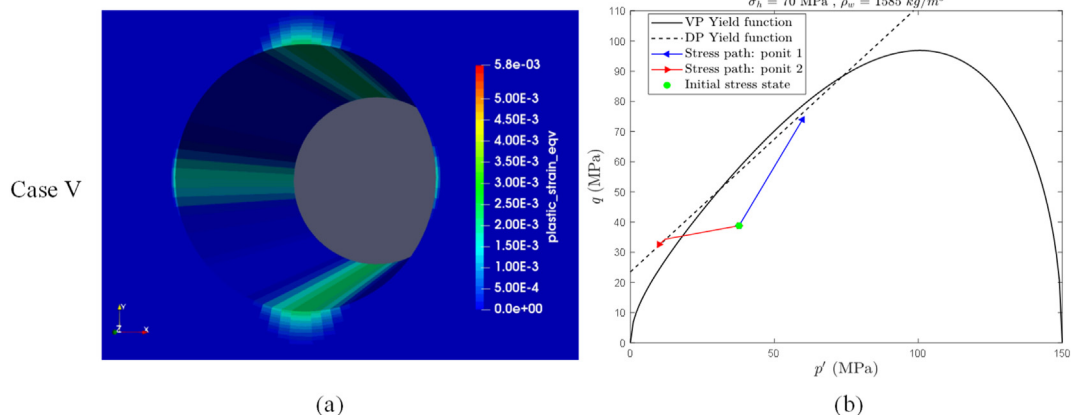

(a)

(b)

Fig. 11. Plots showing the simulation results by using DP model: (a) accumulated plastic equivalent strain and (b) stress paths of the selected points.

with a different set of in-situ stress (case IV: the minimum horizontal stress is decreased from 81 to 70 MPa) to demonstrate the change in the produced plastic zone. The results of plastic zone and stress paths of key monitoring points are displayed in Fig. 9. The transition of in situ stress is accompanied by an increase in the deviatoric part of the effective stress tensor, which leads to the development of localized plastic shear zone. For this case, the initial stress state is closer to the yield surface, and plastic zones are developed around both point 1 and point 2, which can be demonstrated in the stress path curves (Fig. 9). In particular, the zone around point 2 displays a trend of developing tensile stress to approach the yield locus. Our simulation demonstrates the significant impact of in-situ stress on the plastic zone development around a wellbore.

5.2. Comparison with cases using traditional plastic model

Traditional plastic models (e.g., Drucker-Prager model and Mohr-Coulomb model) are also frequently considered in poromechanical analysis of wellbore stability (Li et al., 2018) due to their convenience. The Drucker–Prager yield envelope is a smoother version of the classical Mohr-Coulomb failure criterion and the parameters conversion should be carried out based on matching yielding curves in the meridian plane at different Lode angles (Drucker, 1950; Jiang and Xie, 2011; Puzrin, 2012). The Drucker–Prager yield criterion is concisely expressed as:

$$q - p^{'}\tan\beta - d = 0 \tag{23}$$

where β is the rock's friction angle based on Drucker–Prager model and d is the corresponding cohesion strength.

We also have conducted numerical simulations using the previously mentioned FEM package for a case using Drucker-Prager (DP) criteria and investigated the difference in generating plastic zones (Table 5). After taking four tests' peak strengths, we obtained the strength parameters after displaying strength measurement in equivalent mean stress-equivalent shear stress ($p^{'} - q$ stress space) and fitting the measured results with the linear Drucker-Prager model. Before the field scale simulation, triaxial numerical tests were also conducted as a calibration to obtain critical mechanical parameters. Modeled stress-strain curves at different confining pressures are shown in Fig. 10. For an axial strain lower than 0.6%, the samples display a linear elastic trend. The strain hardening effect is noticed when the applied stress is beyond the yield limit, which is also an indication of high plastic behavior in such high confining pressure conditions. While using the traditional Drucker-Prager, the numerical tests cannot capture the strain softening behavior. Thus, there are major differences in the stress-strain relations among measured and modeled results in the post-peak softening stage. It should also be noted that a lower bound of strength has been selected for matching the stress-strain curves.

For the field scale analysis, we carried out Case IV using DP model with same in-situ stress condition as of Case IV (Table 5). Similarly, the results of plastic zones and stress path curves are shown in Fig. 11. Compared to the results from Cases IV, there are much less plastic zone developed. Even though the calibration has been conducted from a conservative side, there is still less plastic strain both in terms of magnitude and plastic zone size. In a future poromechanical analysis related to hydraulic fracturing processes, where compaction to dilation transition is more important (Chen et al., 2020), our model is potentially giving more reasonable results for fracturing design and injection optimization.

5.3. Advantages and limitations of the study

In the present study, the constitutive modelling is carried out based on a thermomechanics-based viscoplastic model implemented using the finite element method. The advantage is that both laws of thermodynamics and non-associated flow rule are fulfilled. With the increase of confining pressures, the transition from shear dilation to volumetric compression can be well characterized. All the model parameters have clear physical meanings and can be conveniently obtained based on traditional triaxial tests. From the laboratory to the borehole scale, the simulation tasks can be completed in several hours using a standard desktop computer. If the modeling approach is applied to simulate regional-scale numerical analysis like basin compaction process or in-situ stress changes due to geo-energy productions, which requires a super large computing capacity, the scalability of the numerical framework will be an important asset. However, the present simulation only provides the developed plastic zone around a wellbore. The whole borehole failure process cannot be well captured. The Discrete Element based models (DEM) are also commonly used to simulate the poromechanical response of boreholes (Li and Zhang, 2022), and the micro-scale failure mechanisms can be well captured. However, DEM simulations required more calibrated parameters. There is a trade-off between FEM-based and DEM-based modelling, and the choice of the numerical method depends on the specific demand and the goal of the analysis.

6. Conclusions

In this study, we applied a thermomechanics-based viscoplastic model to simulate the stress-strain characteristics of a laumontite-rich tight rock. The constitutive modeling scheme is further included in the poromechanical analysis of deeply drilled wells in an over pressured reservoir for tight oil production. Several conclusions are drawn as the following:

- Petrophysical characterizations on mineral compositions and microstructures of the glutenite cores show that the dominant mineral is laumontite and pore space is mainly aligned around large aggregates. The highly porous and heterogeneity characteristics of the studying laumontite-rich tight rock formation contribute to its strong confining pressure dependent mechanical behaviors.
- Under a low confining pressure, the laumontite-rich tight rock displays a strain hardening followed by post-peak softening behavior. With an increase of the confining pressure, there is a transition from dilation to compression regime. The complicated constitutive behavior can be well quantified by using the thermomechanics-based viscoplastic model, where both laws of thermodynamics and non-associated flow rule are fulfilled.
- The finite element numerical modeling of the plastic zone development around a borehole drilled in an over pressured reservoir shows the advantage of the applied thermomechanics-based viscoplastic model. The modeling scheme used in this study is potentially applicable to other soft rock formations involved other deep geo-energy production or geological engineering projects.

Declaration of competing interest

The authors declare that they have no known competing financial interests or personal relationships that could have appeared to influence the work reported in this paper.

Appendix. Single-Porosity Poroelastic Solution

The analytical solutions of $\sigma_{rr}^{(1)}, \sigma_{rr}^{(2)}, \sigma_{rr}^{(3)}, \sigma_{\theta\theta}^{(1)}, \sigma_{\theta\theta}^{(2)}, \sigma_{\theta\theta}^{(3)}, p_f^{(2)}$, and $p_f^{(3)}$ in the Laplace domain are given as follows (Abousleiman and Nguyen, 2005)

$$\overline{\sigma}_{rr}^{(1)} = (\sigma_m - p_w)\frac{R^2}{r^2}H(t) \tag{A1}$$

$$\overline{\sigma}_{\theta\theta}^{(1)} = -(\sigma_m - p_w)\frac{R^2}{r^2}H(t) \tag{A2}$$

$$\overline{\sigma}_{rr}^{(2)} = -\frac{2\chi_t}{s}(p_o - p_w)\left[\frac{K_1[\xi r]}{\xi r K_0[\xi R]} - \frac{R K_1[\xi R]}{\xi r^2 K_0[\xi R]}\right] \tag{A3}$$

$$\overline{\sigma}_{\theta\theta}^{(2)} = \frac{2\chi_t}{s}(p_o - p_w)\left[\frac{K_0[\xi r]}{K_0[\xi R]} + \frac{K_1[\xi r]}{\xi r K_0[\xi R]} - \frac{R K_1[\xi R]}{\xi r^2 K_0[\xi R]}\right] \tag{A4}$$

$$\overline{\sigma}_{rr}^{(3)} = \frac{\sigma_d}{s}\left[C_1\left(\frac{1}{\xi r}K_1[\xi r] + \frac{6}{(\xi r)^2}K_2[\xi r]\right) - C_2\frac{R^2}{r^2} - 3C_3\frac{R^4}{r^4}\right]\cos(2\theta) \tag{A5}$$

$$\overline{\sigma}_{\theta\theta}^{(3)} = \frac{\sigma_d}{s}\left[-C_1\left(\frac{1}{\xi r}K_1[\xi r] + \left(1 + \frac{6}{(\xi r)^2}\right)K_2[\xi r]\right) + 3C_3\frac{R^4}{r^4}\right]\cos(2\theta) \tag{A6}$$

$$\overline{p}_f^{(2)} = -\frac{(p_o - p_w)}{s}\frac{K_0[\xi r]}{K_0[\xi R]} \tag{A7}$$

$$\overline{p}_f^{(3)} = \frac{\sigma_d}{2s}\left[\frac{C_1}{\chi_t}K_2[\xi r] + \frac{fC_2}{Gh/K_v + 1}\frac{R^2}{r^2}\right]\cos(2\theta) \tag{A8}$$

Where G is the shear modulus, $H(t)$ is the Heaviside unit step function, s is the Laplace transform variable, $\overline{\bullet}$ denotes the Laplace transformation, and K_n is the modified Bessel function of the second kind of nth order.

$$\xi = \sqrt{\frac{s}{c}} \tag{A9}$$

In which c is the diffusion coefficient given as:

$$\frac{1}{c} = \frac{1}{\mathcal{K}M_b} + \frac{\alpha_B^2}{\mathcal{K}K_v} \tag{A10}$$

Where $\mathcal{K}$ is the fluid mobility which can be obtained by permeability and viscosity:

$$\mathcal{K} = \frac{k}{\mu_f} \tag{A11}$$

K_v is the elastic constant defined as:

$$K_v = K + \frac{4}{3}G \tag{A12}$$

The material coefficients can be found by:

$$\chi_t = \alpha_B\frac{1 - 2\nu}{2(1 - \nu)} \tag{A13}$$

$$f = \frac{\alpha_B c}{\mathcal{K}K_v} \tag{A14}$$

$$h = \alpha_B f - 1 \tag{A15}$$

$$C_1 = -4f\chi_t \frac{\xi R}{D_2 - D_1},$$

$$C_2 = \frac{4D_2}{D_2 - D_1},$$

$$C_3 = -\frac{\xi R(D_2 + D_1) + 8f\chi_t K_2[\xi R]}{\xi R(D_2 - D_1)}$$

(A16)

With

$$D_1 = 2f\chi_t K_1[\xi R],$$
$$D_2 = \xi R(Gh/K_v + 1)K_2[\xi R]$$

(A17)

References

Abaqus, 2016. Abaqus Theory Manual. Simulia, Version 6.16.

Abdollahipour, A., Soltanian, H., Pourmazaheri, Y., Kazemzadeh, E., Fatehi-Marji, M., 2019. Sensitivity analysis of geomechanical parameters affecting a wellbore stability. J. Cent. South Univ. 26, 768–778. https://doi.org/10.1007/s11771-019-4046-2.

Abousleiman, Y., Nguyen, V., 2005. Poromechanics response of inclined wellbore geometry in fractured porous media. J. Eng. Mech. 131, 1170–1183.

An, M., Zhang, F., Min, K., Elsworth, D., Marone, C., He, C., 2021. The potential for low-grade metamorphism to facilitate fault instability in a geothermal reservoir. Geophys. Res. Lett. 48, e2021GL093552.

Baik, M., Lee, S., Shon, W., 2009. Retention of uranium (VI) by laumontite, a fracture-filling material of granite. J. Radioanal. Nucl. Chem. 280, 69–77.

Biot, M.A., 1956. General Solutions of the Equations of Elasticity and Consolidation for a Porous Material.

Bravo, A., Jerez, O., Kelm, U., Poblete, M., 2017. Dehydration-hydration reactivity of laumontite: analyses and tests for easy detection. Clay Miner. 52, 315–327.

Chen, B., Xu, B., Li, B., Kong, M., Wang, W., Chen, H., 2020. Understanding the performance of hydraulically fractured wells in the laumontite-rich tight glutenite formation. J. Pet. Sci. Eng. 185. https://doi.org/10.1016/j.petrol.2019.106600.

Chen, S., Xiang, H., Li, B., Xu, B., 2022. Geomechanical dilation assisted VHSD process in altered-stress mature oilsands reservoir: geomechanical studies and field experiences. In: 56th US Rock Mechanics/Geomechanics Symposium. OnePetro.

Chen, S.L., Abousleiman, Y.N., Muraleetharan, K.K., 2012. Closed-form elastoplastic solution for the wellbore problem in strain hardening/softening rock formations. Int. J. GeoMech. 12, 494–507.

Collins, I.F., 2003. A systematic procedure for constructing critical state models in three dimensions. Int. J. Solid Struct. 40, 4379–4397.

Cui, L., Cheng, A.H.D., Abousleiman, Y., 1997. Poroelastic Solution for an Inclined Borehole.

Drucker, D.C., 1950. Some implications of work hardening and ideal plasticity. Q. Appl. Math. 7, 411–418.

Evans, J.P., Chester, F.M., 1995. Fluid-rock interaction in faults of the San Andreas system: inferences from San Gabriel fault rock geochemistry and microstructures. J. Geophys. Res. Solid Earth 100, 13007–13020.

Heidari, S., Li, B., Zsaki, A.M., Xu, B., Wang, C., 2021. Stability analysis of a super deep petroleum well drilled in strike-slip fault zones in the Tarim Basin, NW China. Arabian J. Geosci. 14, 675. https://doi.org/10.1007/s12517-021-06709-z.

Hu, M., Veveakis, M., Regenauer-Lieb, K., 2018. Influence of stress field anisotropy on drilling-induced tensile fracture. Environ. Geotech. 7, 373–379.

Jacquey, A.B., Regenauer-Lieb, K., 2021. Thermomechanics for geological, civil engineering and geodynamic applications: rate-dependent critical state line models. Rock Mech. Rock Eng. 54, 5355–5373.

Jacquey, A.B., Regenauer-Lieb, K., Cacace, M., 2021. Thermomechanics for geological, civil engineering and geodynamic applications: numerical implementation and application to the Bentheim sandstone. Rock Mech. Rock Eng. 54, 5337–5354.

Jiang, H., Xie, Y., 2011. A note on the mohr–coulomb and drucker–prager strength criteria. Mech. Res. Commun. 38, 309–314.

Li, B., Wong, R.C.K., 2017. A mechanistic model for anisotropic thermal strain behavior of soft mudrocks. Eng. Geol. 228. https://doi.org/10.1016/j.enggeo.2017.08.008.

Li, B., Wong, R.C.K., Xu, B., Yang, B., 2018. Comprehensive stability analysis of an inclined wellbore embedded in Colorado shale formation for thermal recovery. Int. J. Rock Mech. Min. Sci. https://doi.org/10.1016/j.ijrmms.2018.07.019.

Li, M., Zhang, F., 2022. Discrete element modeling of hydraulic fracturing. In: Mechanics of Hydraulic Fracturing, pp. 141–175. https://doi.org/10.1002/9781119742487.ch12.

Liu, J.G., Xu, B., Sun, L., Li, B., Wei, G.J., 2022. In situ stress field in the Athabasca oil sands deposits: field measurement, stress-field modeling, and engineering implications. J. Pet. Sci. Eng. 215, 110671. https://doi.org/10.1016/j.petrol.2022.110671.

Ma, X., Zhang, S., Zhang, X., Liu, J., Jin, J., Cheng, W., Jiang, W., Zhang, G., Chen, Z., Zoback, M.D., 2022. Lithology-controlled stress variations of Longmaxi shale – example of an appraisal wellbore in the Changning area. Rock Mech. Bull. 1, 100002. https://doi.org/10.1016/j.rockmb.2022.100002.

Morrow, C.A., Byerlee, J.D., 1991. A note on the frictional strength of laumontite from Cajon Pass, California. Geophys. Res. Lett. 18, 211–214.

Mukherjee, M., Nguyen, G.D., Mir, A., Bui, H.H., Shen, L., El-Zein, A., Maggi, F., 2017. Capturing pressure- and rate-dependent behaviour of rocks using a new damage-plasticity model. Int. J. Impact Eng. 110, 208–218. https://doi.org/10.1016/j.ijimpeng.2017.01.006.

Puzrin, A., 2012. Constitutive Modelling in Geomechanics: Introduction. Springer Science & Business Media.

Solum, J.G., van der Pluijm, B.A., Peacor, D.R., Warr, L.N., 2003. Influence of phyllosilicate mineral assemblages, fabrics, and fluids on the behavior of the Punchbowl fault, southern California. J. Geophys. Res. Solid Earth 108. https://doi.org/10.1029/2002JB001858.

Stehfest, H., 1970. Algorithm 368: numerical inversion of Laplace transforms [D5]. Commun. ACM 13, 47–49.

Vermeer, P.A., De Borst, R., 1984. Non-associated plasticity for soils, concrete and rock. Heron 29 (3), 1984.

Vernik, L., 1990. A new type of reservoir rock in volcaniclastic sequences. Am. Assoc. Petrol. Geol. Bull. 74, 830–836.

Vernik, L., Nur, A., 1992. Petrophysical analysis of the Cajon Pass scientific well: implications for fluid flow and seismic studies in the continental crust. J. Geophys. Res. Solid Earth 97, 5121–5134.

White, C.L.I.M., Ruiz-Salvador, A.R., Lewis, D.W., 2004. Pressure-induced hydration effects in the zeolite laumontite. Angew. Chem. 116, 475–478.

Wu, H., Zhao, J., Guo, N., 2018. Multiscale insights into borehole instabilities in high-porosity sandstones. J. Geophys. Res. Solid Earth 123, 3450–3473.

Yang, S., Jin, Y., Lu, Y., Zhang, Y., Chen, B., 2021. Performance of hydraulically fractured wells in Xinjiang oilfield: experimental and simulation investigations on laumontite-rich tight glutenite formation. Energies 14, 1667.

Zhang, F., Huang, R., An, M., Min, K., Elsworth, D., Hofmann, H., Wang, X., 2022. Competing controls of effective stress variation and chloritization on friction and stability of faults in granite: implications for seismicity triggered by fluid injection. J. Geophys. Res. Solid Earth 127, e2022JB024310.

Zhang, Y., Ding, X., Yang, P., Liu, Y., Jiang, Q., Zhang, S., 2016. Reservoir formation mechanism analysis and deep high-quality reservoir prediction in Yingcheng Formation in Longfengshan area of Songliao Basin, China. Petroleum 2, 334–343. https://doi.org/10.1016/j.petlm.2016.09.003.

Zheng, Z., Su, G., Jiang, Q., Pan, P., Huang, X., Jiang, J., 2022a. Mechanical behavior and failure mechanisms of cylindrical and prismatic rock specimens under various confining stresses. Int. J. Damage Mech. 31, 864–881.

Zheng, Z., Su, H., Mei, G., Cao, Y., Wang, W., Feng, G., Jiang, Q., 2022b. Experimental and damage constitutive study of the stress-induced post-peak deformation and brittle–ductile behaviours of prismatic deeply buried marble. Bull. Eng. Geol. Environ. 81, 427.

Zhu, C., Arson, C., 2014. A thermo-mechanical damage model for rock stiffness during anisotropic crack opening and closure. Acta Geotech 9, 847–867. https://doi.org/10.1007/s11440-013-0281-0.

Zhu, Q., Shao, J., 2017. Micromechanics of rock damage: advances in the quasi-brittle field. J. Rock Mech. Geotech. Eng. 9, 29–40.